

# First Year Progress Report: Structural and Electronic Properties of InN Surfaces and Interfaces



THE UNIVERSITY OF  
WARWICK

**Liam Fishwick**

Surface, Interface and Thin Film Group, Dept. of Physics, The University of  
Warwick, Coventry, CV4 7AL

Supervisor: Prof. C. F. McConville

## Abbreviations

AES	Auger Electron Spectroscopy
CAICISS	Co-axial Impact Collision Ion Scattering Spectroscopy
CB	Conduction Band
CBM	Conduction Band Minimum
CNL	Charge Neutrality Level
DFT	Density Function Theory
DOS	Density of States
DRS	Direct Recoil Spectroscopy
EELS	Electron Energy Loss Spectroscopy
HREELS	High Resolution Electron Energy Loss Spectroscopy
ICISS	Impact Collision Ion Scattering Spectroscopy
IPES	Inverse Photoemission Spectroscopy
LDA	Local Density Approximation
LEED	Low Energy Electron Diffraction
LEIS	Low Energy Ion Scattering
MEIS	Medium Energy Ion Scattering
NCESS	National Centre for Electron Spectroscopy and Surface analysis
RBS	Rutherford Back Scattering
RHEED	Reflection High Energy Electron Diffraction
TOF	Time of Flight
UPS	Ultra-Violet Photoelectron Spectroscopy
VB	Valence Band
VBM	Valence Band Maximum
XPS	X-ray Photoelectron Spectroscopy

# Contents

<b>Abbreviations</b>	<b>2</b>
<b>1 Introduction</b>	<b>4</b>
<b>2 Background Theory</b>	<b>5</b>
2.1 Semiconductor Bandstructure . . . . .	5
2.1.1 Parabolic approximation . . . . .	5
2.1.2 <b>k.p</b> perturbation theory . . . . .	6
2.2 Surface Science . . . . .	7
2.2.1 Wood Notation . . . . .	7
2.2.2 Ewald sphere construction . . . . .	9
2.3 Techniques . . . . .	10
2.3.1 X-ray Photoelectron Spectroscopy (XPS) . . . . .	10
2.3.2 Low Energy Electron Diffraction (LEED) . . . . .	11
2.3.3 Basics of ion scattering . . . . .	12
2.3.4 Interaction Potentials . . . . .	13
2.3.5 Low Energy Ion Scattering . . . . .	14
<b>3 Instrumentation</b>	<b>17</b>
3.1 CAICISS . . . . .	17
3.1.1 Ion Column . . . . .	17
3.1.2 Main Chamber . . . . .	19
3.2 ELVIS . . . . .	20
<b>4 Current Results</b>	<b>21</b>
4.1 Valence band offsets of ScN systems . . . . .	21
4.1.1 XPS observations . . . . .	21
4.2 CAICISS simulation . . . . .	23
<b>5 Research Plan</b>	<b>25</b>
5.1 April 2009 – June 2009 . . . . .	25
5.2 July 2009 – Sept 2009 . . . . .	25
5.3 Oct 2009 – Dec 2009 . . . . .	25
<b>A Key Text Review</b>	<b>26</b>
A.1 Intrinsic electron accumulation at clean InN surfaces . . . . .	27
A.2 Origins of Fermi-level pinning on GaN and InN polar and nonpolar surfaces	27
A.3 In-adlayers on nonpolar and polar InN surfaces: Ion scattering and photoemission studies . . . . .	29
A.4 Structure of GaN(0001): The laterally contracted Ga bi-layer model . .	30
A.5 Low energy ion scattering at surfaces . . . . .	31
<b>References</b>	<b>33</b>

# 1 Introduction

The recent downward revision of the band gap of InN from 1.4 to  $\sim 0.7$  eV [1, 2], has led to an increasing amount of interest for use within devices and other applications [3]. For the potential of devices to be realised the properties of InN need to be well understood. Particular properties of interest are the location of the branch point energy within InN [4], and the exhibition of an electron accumulation layer at the surface [5], in contrast to the electron depletion layer as observed in GaN [6].

Previous PhD theses produced in the surface interface and thin film group have reported the electronic properties of InN and its alloys in detail. Alloys with GaN are interesting because they provides a tunable band gap which encompasses the entire visible spectrum [7, 8], allowing for the creation of more efficient solar cells.

For InN to be useful in devices methods of contacting the surface need to be developed. It will be important to know the effect on the surface that these contacts have. Any surface reconstructions that are formed as a result of deposition of the contact, or any corresponding changes to the electronic properties will have an effect on the device's usefulness.

Whilst these previous projects have led to an understanding of electronic properties of InN, the knowledge of the structural properties of the clean surface are still not fully understood. Some previous ion scattering studies on c-plane InN grown upon sapphire substrates have been performed [9, 10].

The work in this project is designed to continue the electronic characterisation of InN thin films, utilising techniques including XPS, LEED, Hall effect measurements and other complementary electronic techniques. To further investigate the structural properties of InN, CAICISS will be used to quantitatively characterise the surface of both clean and adsorbate covered InN surfaces, to allow for further progress in development of contacts to surfaces of InN for use within devices.

## 2 Background Theory

### 2.1 Semiconductor Bandstructure

The Schrödinger equation (Equation 2.1) fully describes the behaviour of electrons in solids, when an appropriate Hamiltonian is used.

$$H|\psi\rangle = E|\psi\rangle \quad (2.1)$$

A Hamiltonian that fully describes the system requires the inclusion of the interaction between electrons and ions, and is given by

$$H = \sum_i \frac{\mathbf{p}_i^2}{2m_e} + \sum_j \frac{\mathbf{p}_j^2}{2M_l} + \sum_{i,l} V(\mathbf{r}_i - \mathbf{R}_l) + \sum_{l,m} U(\mathbf{R}_l - \mathbf{R}_m) + \sum_{i,j} \frac{e^2}{4\pi\epsilon_0} \frac{1}{|\mathbf{r}_i - \mathbf{r}_j|} \quad (2.2)$$

Where  $m_e$  is the electron mass,  $M_l$  is the ion mass and  $\mathbf{R}$  is the separation of the ion / electron. Solving this directly would prove to be extremely difficult, so approximations are employed to simplify the process. The key ones in use are the Born-Oppenheimer approximation, mean-field approximation and one electron approximation.

The Born-Oppenheimer approximation [11] states that the electrons are assumed to react instantly to the motion of the ions, but the reaction of ions is much slower, thus allowing us to ignore the motion of the ions. The one electron approximation [11] assumes all electron-electron interactions are averaged, and the mean-field approximation [11] states that all the electrons are in identical surroundings with regards to the ions and their equilibrium positions. These approximations allow us to use a simplified Hamiltonian

$$H = \frac{\mathbf{p}^2}{2m_e} + V_0(\mathbf{r}) \quad (2.3)$$

$V_0(\mathbf{r})$  represents the periodic potential in the lattice, utilising the translational symmetry that is present.

#### 2.1.1 Parabolic approximation

By considering the electron energy dispersion only around the  $\Gamma$ -point (centre of the Brillouin zone) we arrive at an equation for the parabolic approximation at the extrema of the conduction and valence bands (which are in general located at the  $\Gamma$ -point for semiconductors). This can be shown to be [11]

$$E_{e,h}(\mathbf{k}) = E_{e,h}(0) \pm \frac{\hbar^2 \mathbf{k}^2}{2m^*} \quad (2.4)$$

For large gap semiconductors this equation tends to hold well, but this proves to be ineffective for narrow gap semiconductors such as InN, because the interaction between conduction and valence bands cannot be ignored. In this case Kane's  $\mathbf{k}\cdot\mathbf{p}$  perturbation theory [12]  $\mathbf{k}\cdot\mathbf{p}$  is used.

### 2.1.2 $\mathbf{k}\cdot\mathbf{p}$ perturbation theory

Since we are interested in the detailed structure of the bands at their extrema (typically at the  $\Gamma$ -point). The  $\mathbf{k}\cdot\mathbf{p}$  perturbation uses the fact that the cell periodic functions for the electrons for any  $\mathbf{k}$  form a complete set. The wave function used for this can be written as:

$$\psi = u_{n\mathbf{k}}(\mathbf{r}) \exp(i\mathbf{k} \cdot \mathbf{r}) = \left[ \sum c_m U_{m\mathbf{k}_0}(r) \right] \exp(i\mathbf{k} \cdot \mathbf{r}) \quad (2.5)$$

Using  $\psi$  in the Schrödinger equation (Equation 2.1), and the fact that the wave function for  $\mathbf{k} = \mathbf{k}_0$  in the  $n^{\text{th}}$  band is  $\psi = \exp(i\mathbf{k}_0 \cdot \mathbf{r}) U_{m\mathbf{k}_0}(\mathbf{r})$  should produce [13]:

$$\left[ -\frac{\hbar^2}{2m_0} \nabla^2 + \frac{\hbar}{m_0} \mathbf{k}_0 \cdot \mathbf{p} + \frac{\hbar^2 k_0^2}{2m_0} + V(\mathbf{r}) \right] U_{m\mathbf{k}_0}(r) = E_m(\mathbf{k}_0) U_{m\mathbf{k}_0}(\mathbf{r}) \quad (2.6)$$

By using  $\mathbf{p} = -i\hbar\nabla$  we can reduce this equation to the form:

$$\left[ \frac{1}{2m} (\mathbf{p} + \hbar\mathbf{k})^2 + V(\mathbf{r}) \right] U_{n\mathbf{k}} = E_{n\mathbf{k}} U_{n\mathbf{k}} \quad (2.7)$$

To describe the doubly degenerate conduction band and three valence bands as originally performed by Kane[12] with zinc blende structures (i.e. no crystal field splitting), we are lead to a Hamiltonian of the form

$$H = \begin{pmatrix} \tilde{H} & 0 \\ 0 & \tilde{H} \end{pmatrix} \quad (2.8)$$

where

$$\tilde{H} = \begin{pmatrix} E_s & 0 & kP & 0 \\ 0 & E_p - \Delta_{so}/3 & \sqrt{2}\Delta_{so}/3 & 0 \\ kP & \sqrt{2}\Delta_{so}/3 & E_p & 0 \\ 0 & 0 & 0 & E_p + \Delta_{so}/3 \end{pmatrix} \quad (2.9)$$

Here  $E_s$  and  $E_p$  are the eigenvalues of the Hamiltonian at the  $\Gamma$ -point and  $P$  is

Kane's matrix element [14], which is given by

$$P^2 = \frac{3\hbar^2 \left( \frac{1}{m_0^*} - \frac{1}{m_0} \right)}{2 \left[ \frac{2}{E_g} + \frac{1}{(E_g + \Delta_{so})} \right]} \quad (2.10)$$

In the limit  $\Delta_{so} \ll E_g$ , the spin-orbit splitting can be neglected and Equation 2.9 reduces to a  $2 \times 2$  matrix of the form

$$H = \begin{pmatrix} E_s & kP \\ kP & E_p \end{pmatrix} \quad (2.11)$$

Solving the Schrödinger equation for this Hamiltonian leads to the  $\alpha$ -approximation, describing the conduction band in Equation 2.12.

$$E(1 + \alpha E) = \hbar^2 \left( \frac{1}{m^*} - \frac{1}{m_0} \right) \frac{E_g}{2} \quad (2.12)$$

Where  $\alpha = \frac{1}{E_g}$  and  $E$  is measured from the conduction band minimum. Valence electrons can also be described by a similar method.

## 2.2 Surface Science

A surface is a special kind of defect, where the bulk structure of the material terminates with the vacuum. In most materials this causes a re-arrangement of the top few layers of atoms to minimise the energy of the structure. This re-arrangement is known as a relaxation, and can take the form of a contraction or expansion of the top few layers of atoms with respect to the surface. The minimisation of energy is also what leads to surface reconstructions that are observed for many materials, such as a  $(2 \times 2)$  reconstruction on the surface of GaN.

### 2.2.1 Wood Notation

For an ordered crystal surface it is convenient to describe the order by relating its Bravais net to that of the underlying substrate as shown in Equation 2.13

$$\begin{aligned} \mathbf{a}' &= G_{11}\mathbf{a} + G_{12}\mathbf{b} \\ \mathbf{b}' &= G_{21}\mathbf{a} + G_{22}\mathbf{b} \end{aligned} \quad (2.13)$$

Where  $\mathbf{a}$  and  $\mathbf{b}$  are the vectors of the substrate,  $\mathbf{a}'$  and  $\mathbf{b}'$  are those of the adsorbate or selvage, and  $G_{ij}$  are the coefficients forming a matrix  $G$  (Equation 2.14) which relates the adsorbate and substrate meshes (Equation 2.15).

$$G = \begin{pmatrix} G_{11} & G_{12} \\ G_{21} & G_{22} \end{pmatrix} \quad (2.14)$$

$$\begin{pmatrix} \mathbf{a}' \\ \mathbf{b}' \end{pmatrix} = G \begin{pmatrix} \mathbf{a} \\ \mathbf{b} \end{pmatrix} \quad (2.15)$$

The matrix  $G$  as shown in Equation 2.14 is the matrix notation used for describing surface structures. The second, less versatile but somewhat more convenient method for describing a surface is Wood notation. In Wood notation a structure can be referred to as:

$$X\{hkl\}(p \times q)R\phi^\circ - A \quad (2.16)$$

This represents an adsorbate  $A$  on the  $\{hkl\}$  surface of material  $X$ , primitive translation vectors  $|\mathbf{a}'| = p|\mathbf{a}|$ ,  $|\mathbf{b}'| = q|\mathbf{b}|$ , unit mesh rotation of  $\phi$ .

Using Figure 2.1 it is possible to explain how the Wood notation is reached.  $a_0$  and  $b_0$  correspond to the lattice vectors of the overlayer, and  $a_s, b_s$  the lattice vectors of the substrate. These can be placed into the matrix notation as described in Equation 2.15, to lead us to Equation 2.17.

$$\begin{pmatrix} a_0 \\ b_0 \end{pmatrix} = \begin{pmatrix} 2 & 0 \\ 0 & 2 \end{pmatrix} \begin{pmatrix} a_s \\ b_s \end{pmatrix} \quad (2.17)$$

The coefficients of the  $G$  matrix correspond to  $p$  and  $q$  values of 2. Now substitute these values into Equation 2.16 and the Wood notation for this structure is shown as Equation 2.18.

$$X\{100\}(2 \times 2) - A \quad (2.18)$$

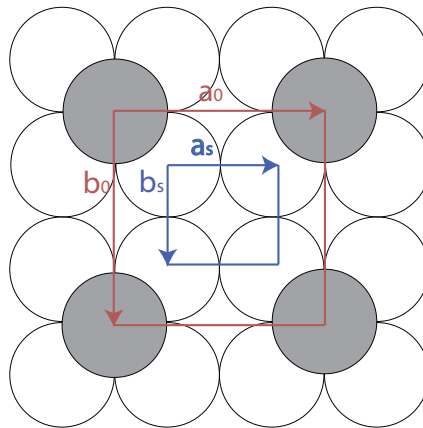


Figure 2.1: Example of 100 plane of fcc substrate  $X$ , with adsorbate  $A$ . The adsorbate is shown in grey, with substrate in white.

### 2.2.2 Ewald sphere construction

A useful aid in determining lattice parameters is the Ewald sphere construction method [15]. The specific application of this method for this project is for use with LEED, which relies on backscattered electrons in the energy range 20 – 100 eV. Electrons in this energy range have a mean free path comparable to the separation of atoms  $\sim 5 - 20 \text{ \AA}$ , which leads to a penetration depth of only a few layers into the surface of a crystal. The de Broglie wavelength of these electrons can be described by Equation 2.19.

$$\lambda(\text{\AA}) = \left( \frac{150.4}{E(\text{eV})} \right)^{\frac{1}{2}} \quad (2.19)$$

Using this result it is possible to determine the incident wavevector

$$|\mathbf{k}_0| = \frac{2\pi}{\lambda} \quad (2.20)$$

In three dimensions (bulk state), the Ewald sphere is populated with spots at specific  $k$  values that satisfy the Bragg condition. In two dimensions (surface state) the Ewald sphere reduces to a circle, with the spots becoming rods that satisfy the Bragg condition. It is now possible to see the relationship between the reciprocal lattice vector  $a^*$  and  $|\mathbf{k}_0|$ :

$$a^* = |\mathbf{k}_0| \sin \theta \quad (2.21)$$

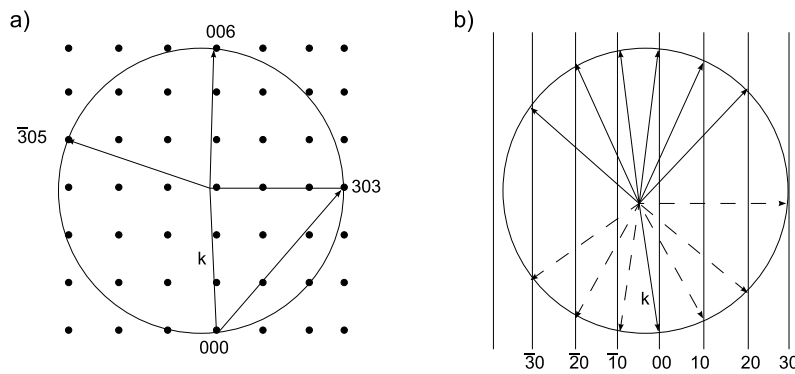


Figure 2.2: Ewald sphere construction for a) bulk and b) surface cases. Incident electron wavevector  $\mathbf{k}$  labelled with possible scattered wavevectors ( $\mathbf{k}'$ ). Dashed wavevectors in b) scatter into crystal and are not observable.

When the reciprocal lattice rods intersect the Ewald sphere, spots will appear in a LEED experiment. Upon changing of energy of the incident beam, the radius of the Ewald sphere changes, causing more or less spots to appear on the screen.

## 2.3 Techniques

The following section discusses the theory behind the important techniques used in this project, for the study of both electrical properties and structural properties of InN and related alloys.

### 2.3.1 X-ray Photoelectron Spectroscopy (XPS)

An X-ray photon of energy  $h\nu$  is incident on a surface and is absorbed by an atom with binding energy  $E_B$ . If the incident energy of the photon is larger than  $E_B$  then the electron is ejected from the atom with energy  $E_k$ . This is then detected in an analyser and the binding energy of that electron is determined by:

$$E_B = h\nu - E_k - \phi_{\text{analyser}} \quad (2.22)$$

where  $\phi_{\text{analyser}}$  is the work function of the electron analyser, not the species in question.

This means that any detected electrons provide a specific fingerprint of the atomic species in the near surface region. Slight variations in the binding energy known as chemical shifts, allow the chemical environment of atoms in the near surface region to be determined. However, due to varying x-ray absorption probabilities of different states the picture is slightly more complex. This process is shown schematically in Figure 2.3.

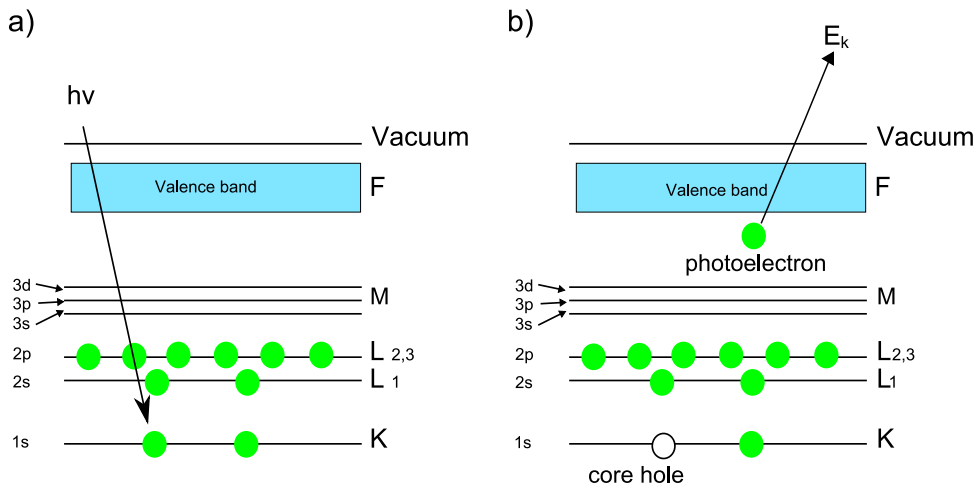


Figure 2.3: Schematic of the photoemission process in XPS. a) Incident photon energy  $h\nu$  is absorbed by a core level electron. b) If  $h\nu > E_B$  then the electron is emitted and a core hole is left behind. This core hole may be filled by an electron from a higher state, causing emission of a secondary photon, or an Auger electron [15].

A typical XPS spectrum is illustrated in Figure 2.4. The spectrum shows a series of sharp peaks corresponding to core states of surface atoms. These peaks are accompanied by inelastic loss tail features, arising from interactions before the electrons

emerge from the surface, thus reducing their energy. This feature in itself can be used to obtain chemical depth profiles of the sample [16].

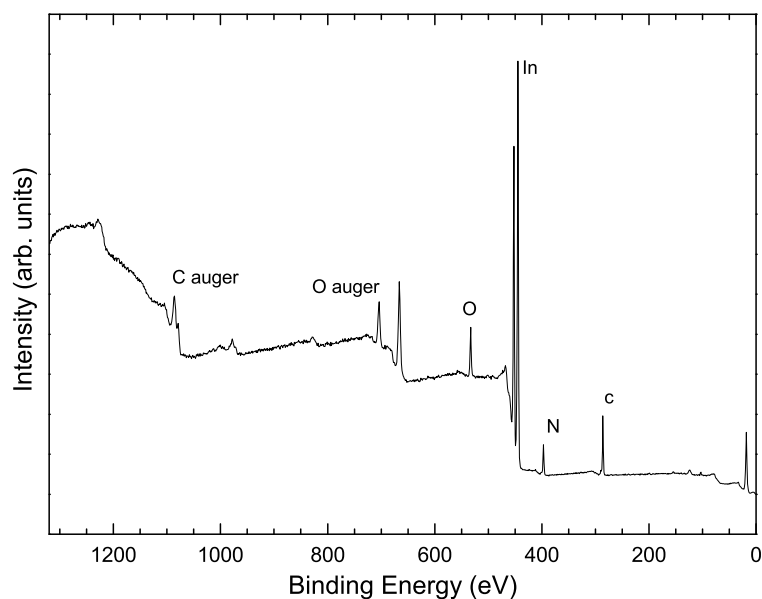


Figure 2.4: A typical XPS spectrum of an as-loaded InN sample, taken with a monochromated 1486.6 eV  $Al_{K\alpha}$  source. Stepped structure of the background is due to inelastic processes.

Increasing the surface specificity of XPS can be achieved by using smaller angles of incidence, to reduce the sampling depth as illustrated in Figure 2.5. For quantitative XPS analysis broadening due to the energy width of electronic state, phonons and the instrumental resolution must be taken into account. Despite this XPS remains an excellent tool for qualitative and quantitative analysis and will thus be used extensively throughout this project.

### 2.3.2 Low Energy Electron Diffraction (LEED)

LEED is based on the principle of conservation of energy and momentum for electrons incident on a sample [15]. An important tool when performing LEED is the Ewald sphere construction, which gives the directions of the diffracted beams that should be experimentally observed. An example LEED pattern is shown in Figure 2.6.

It is possible to obtain quantitative as well as qualitative information about the surface of a crystal in LEED. LEED  $I(V)$  mode can be used to determine atomic positions when compared with simulations [17]. Qualitative LEED, which will be used in this project, is used to check for an ordered surface, where a high background signal, or lack of LEED pattern completely indicates a poor ordering of the surface. This tool will also allow the investigation of any reconstruction present on the surface when materials are deposited onto a clean surface.

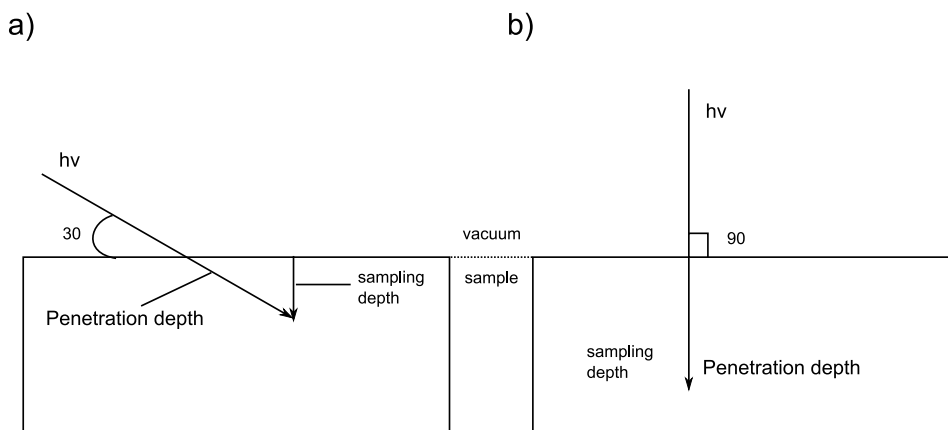


Figure 2.5: Schematic of sampling depth at a) 30° and b) 90°. The lower incidence angle leads to higher surface specificity.



Figure 2.6: Example LEED pattern showing a (1 × 1) reconstruction of a clean InN(0001) surface.

### 2.3.3 Basics of ion scattering

Ion scattering is very useful as the physics that governs the process is relatively simple when compared to that of some other surface techniques. It is a real-space technique, meaning the interpretation of data is much simpler. The ideal scattering process can be described as a binary collision, of the form shown in Figure 2.7, described by Equation 2.23.

$$\frac{E_1}{E_0} = \frac{1}{(1 + A)^2} [\cos \theta_1 \pm (A^2 - \sin^2 \theta_1)^{1/2}]^2 \quad (2.23)$$

Where  $A = \frac{M_2}{M_1}$ ,  $M_1$  is the mass of the incident ion,  $M_2$  is the mass of the target atom,  $E_0$  is the kinetic energy of incident ion,  $E_1$  kinetic energy of scattered ion, and  $\theta_1$  is the scattering angle with respect to incident trajectory[18].

With a monoenergetic incident ion beam, Equation 2.23 shows that with a knowledge of  $\theta_1$ ,  $M_1$ , and  $E_0$ , a measurement of  $E_1$  leads to a determination of the mass of the target atom,  $M_2$ . By picking 180° as the scattering angle it can be seen that

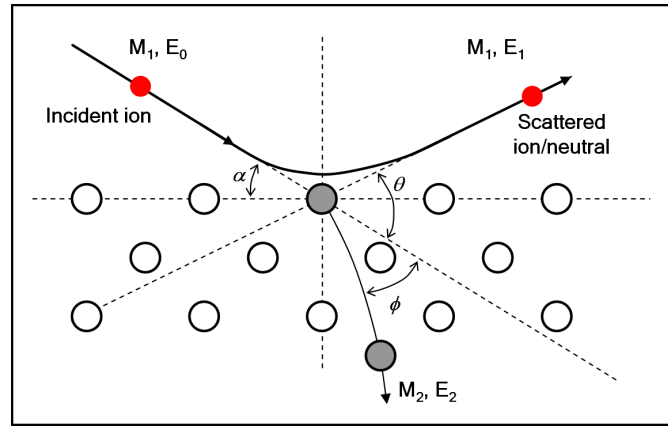


Figure 2.7: Schematic diagram of ion-surface atom binary collision model.

Equation 2.23 simplifies to

$$\frac{E_1}{E_0} = \frac{(A - 1)^2}{(A + 1)^2} \quad (2.24)$$

To obtain quantitative information about the species present at the surface of a material it is necessary to understand the interaction potentials, due to the effects of ion neutralisation and scattering cross-section.

### 2.3.4 Interaction Potentials

Ion scattering is described by a Coulombic interaction of the two particles, but can only be considered to be purely Coulombic at high energies (MeV scale). At low energies, the longer interaction times mean that electron screening must be taken into account. The interaction potential falls off faster than  $\frac{1}{r}$ , with the Coulombic interaction being multiplied by a screening function is commonly used. Such a potential is illustrated in Equation 2.25 [18].

$$V(r) = \frac{Z_1 Z_2 e^2}{4\pi\epsilon_0 r} \phi(r/a) \quad (2.25)$$

Where  $a$  is the screening length, and  $\phi(r/a)$  is the screening function. This potential can be described in two different ways; a Molière approximation to the Thomas-Fermi model [19, 20], or the Ziegler-Biersack-Littmark (ZBL) [21] function, although the ZBL potential has been shown to be inappropriate for CAICISS analysis [22]. Using this the scattering angle  $\theta_1$  and impact parameter  $b$  can be computed, giving a set of trajectories. The Coulombic interaction creates shadow cones behind the target atoms, and any other atom which is in that cone will be sheltered from the flux and thus not contribute to the signal, as shown in Figure 2.8. It can also be seen that at the edge of the shadow cone trajectory focussing occurs, thus increasing detected intensity. At

low incident energies these shadow cones can be a large fraction of the interatomic spacing in the surface region, this is illustrated in Figure 2.9.

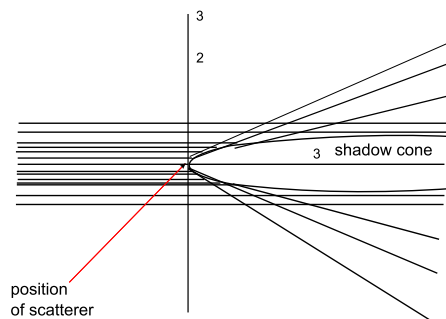


Figure 2.8: Scattering trajectory of an incident ion displaying shadow cones on atoms in following layers.

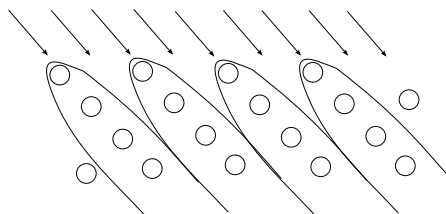


Figure 2.9: Shadow cones from top three layer of atoms on a (100) surface of an ideal crystal.

### 2.3.5 Low Energy Ion Scattering

The use of low energy ions has two advantages for surface studies, high cross-sections for ion-atom interactions and higher neutralisation probabilities for noble gas ions due to reduced velocity. This leads to a sensitivity to only the near surface region ( $\sim 3 - 5$  atomic layers) [15].

Early experiments, such as those performed by Smith [23] suggested LEIS was a good technique for the determination of surface elemental composition. Any ions undergoing multiple scattering events lose energy, whilst deeply penetrating ions are extremely likely to be neutralised [18]. The early detection systems were electrostatic analysers, which would detect scattered ions, thus making LEIS experiments truly surface specific.

In the field of LEIS there are several variations to the technique that have been introduced to address the neutralisation problem, allowing the near surface structure and composition to be studied. These can all be classed as impact collision ion scattering spectroscopy (ICISS). The use of alkali metal ions (ALCISS [18], which have a reduced ionisation probability), detection of neutrals and ions (NICISS [18]), both of

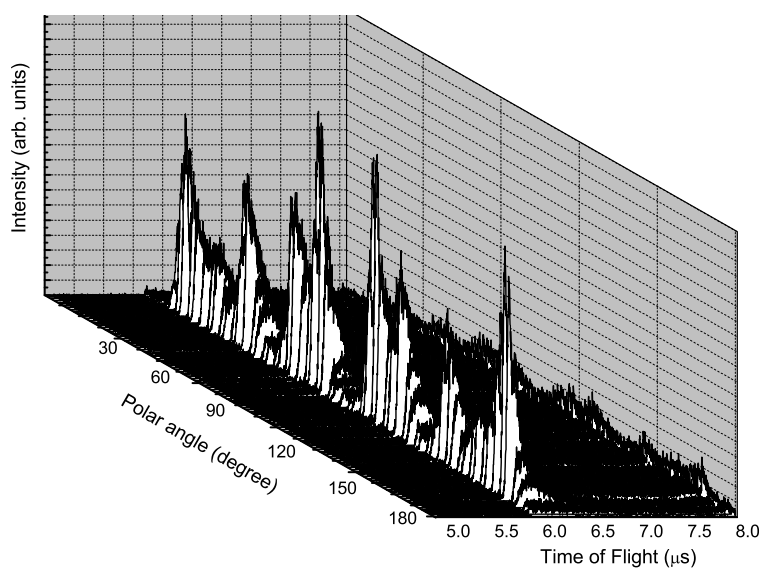


Figure 2.10: Example 3D plot produced by a polar scan, showing counts vs TOF vs polar angle.

which are operated in a time-of-flight (TOF) mode. The TOF mode is useful as any scattered ions will have a reduced velocity due to the energy exchanged in the collision, thus meaning it will have a longer flight time to the detector, but no ions that haven't been scattered make it to the detector.

An interesting variation on this principle is co-axial impact collision ion scattering spectroscopy (CAICISS), which utilises the  $180^\circ$  backscattering geometry. By looking at a specific incidence angle it is possible to build up an intensity profile that can identify the different elemental species in the surface region. If the sample is rotated on the polar axis then a 3D plot (counts vs TOF vs angle) is produced, as shown in Figure 2.10. This is then filtered for each element to give the 2D plot shown in Figure 2.11.

Figure 2.11 shows several important features within the spectrum, particularly for determining structural and chemical makeup of the crystal. Starting at  $0^\circ$ , i.e. parallel to the surface, every atom is in the shadow cone of the previous atom. Increasing the angle of incidence leads to the surface atoms emerging from the shadow cones, until the edge of the cone from one atom is directly focussed on the next atom in the chain, thus producing a large increase in the backscattered ion yield, known as the surface peak and this effect arrives due to trajectory focussing [18]. The relevant angle at which this surface peak arises is known as the critical angle, which is related to the interatomic spacing of the atoms at the surface. This is vitally important for characterisation of the surface.

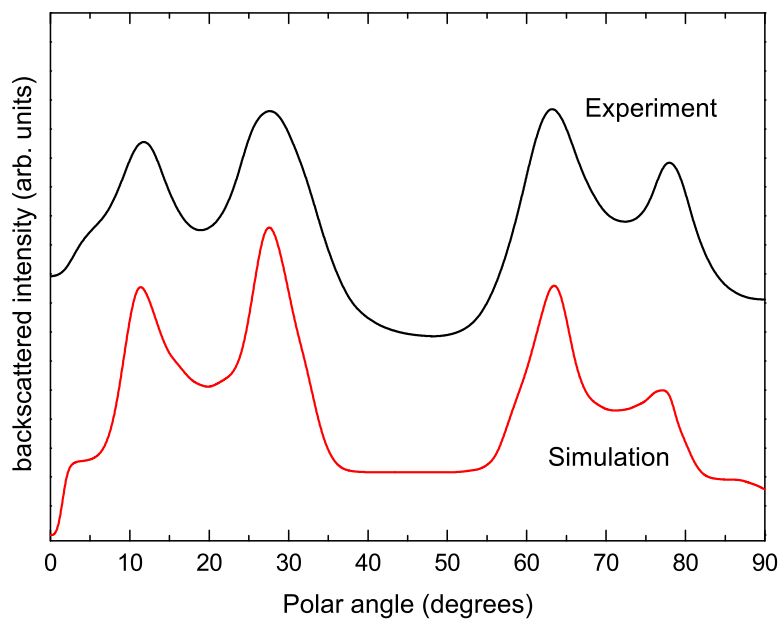


Figure 2.11: Example spectra of a Cu(100) sample for the polar region of 0 – 90°, including the comparison to simulation.

Further increasing the angle of incidence leads to atoms in the second layer emerging from the shadow cones. When the shadow cone is directly focussed on a second layer atom again we see an increase in backscattering yield. This is used to determine interlayer spacing, and can be used to look for surface relaxations, where the topmost interlayer spacing may change from that of the bulk due to effects such as adsorption of other elements onto the surface, or temperature. A similar effect is seen when focussed onto the third layer atoms. Depending on the crystal structure it may be possible to observe contributions from deeper layers.

### 3 Instrumentation

The majority of work for this project will be carried using to vacuum chambers at Warwick. The CAICISS system will be used for structural studies, but is also equipped with LEED, AES, XPS and sample preparation equipment. The ELVIS system will be used for the study of electronic properties of clean and adsorbate covered InN surfaces. External facilities including NCESS (which has high resolution XPS capabilities [24]) and MEIS [25] at Daresbury Laboratory.

#### 3.1 CAICISS

The CAICISS system can be thought of as two separate subsystems. The main chamber where the sample preparation and data acquisition are performed and the ion column that provides a coaxial beam of ions for CAICISS. This modular design has the advantage that change over of samples does not affect the ion column and problems with the ion column will not affect the main chamber.

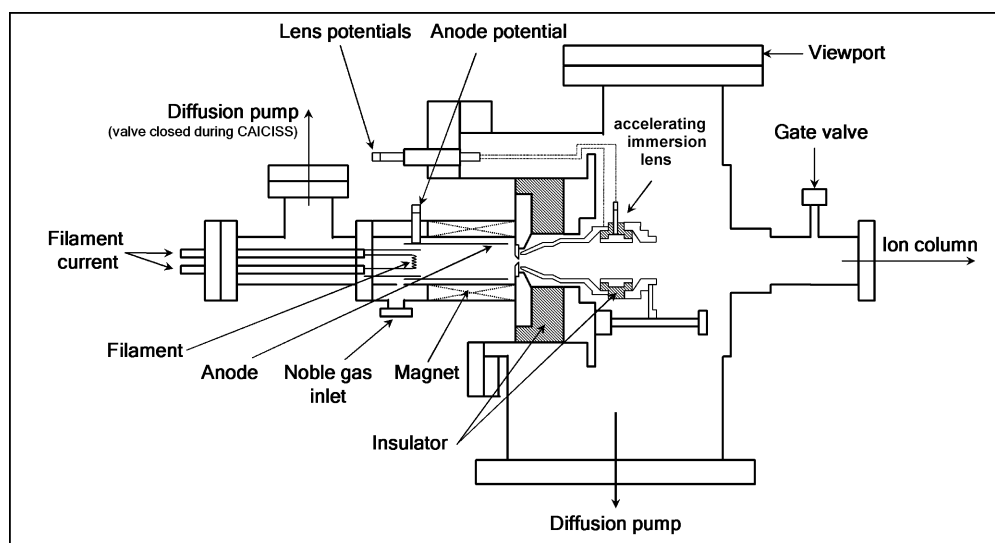


Figure 3.1: Schematic diagram of Nielson ion source [26].

##### 3.1.1 Ion Column

The Nielson ion source as shown in Figure 3.1 produces a high current beam of  $\text{He}^+$  or  $\text{Ne}^+$  ions with very low energy spread. Passing a current of 15A through a Ta filament ejects electrons by thermionic emission. The ion source is filled with a partial pressure of noble gas, which is then ionised by these ejected electrons. A potential difference between the anode and the filament drives the ions through an accelerating

immersion lens and into the column. This lens provides an initial focusing of the beam before entering the column.

Figure 3.2 shows a schematic of the column itself. Upon entering the ions are collimated by an aperture (Col), followed by a series of vertical and horizontal (VSP, HSP) electrostatic deflection plates designed for steering and chopping of the beam. The off-axis port aligned (OAPA) induces a bend in the flight path for charge particles, thus providing a way to removal any remaining neutrals from the beam.

A chopping aperture (ChA) provides a pulsed beam of ions. A periodic voltage is applied to the chopping plates (ChP), causing the beam to be swept across the aperture. The periodic potential is also used to trigger the computerised data acquisition. The period of the chopping potential and sweep time across the ChA determines the time resolution and pulse length of the setup. Typically the pulse length is of the order  $\sim 60$  ns, but can be decreased if studying surfaces with elements close in mass. If studying clean surfaces can be increased to reduce experimental time. The ions are then passed through the centre of a micro-channel plate detector (MCP) and down the remaining section of the column towards the sample. Valves at different points along the column allow for those sections to be isolated when required.

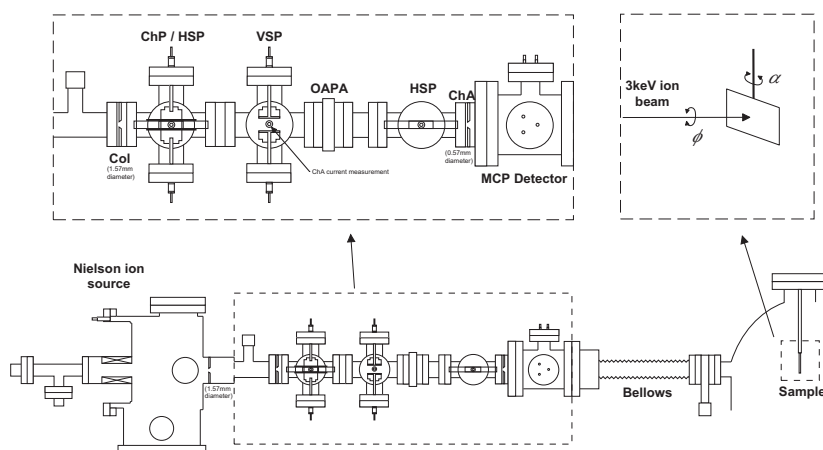


Figure 3.2: Schematic of the ion-source in the Warwick CAICISS system.

Ions are then scattered through  $179 \pm 1^\circ$ , travel back along the column and are detected in the MCP. Because the beam has low energy spread, the TOF of scattered ions depends only on the mass of the scattering surface layer atom. This allows for the masses of scattering atoms in the surface region can be deduced via TOF measurements.

### 3.1.2 Main Chamber

The sample manipulator is capable of both polar and azimuthal sample rotation, and movement in x, y, and z directions with respect to the incoming ion beam. The polar angle rotation is fully automated using an IBM compatible PC and a stepper motor. Each step corresponds to a rotation of  $1.8^\circ$ , whilst azimuthal rotation is still manual. A schematic of the main chamber is shown in Figure 3.3.

The sample holder is capable of heating the sample to  $800^\circ\text{C}$  by direct heating of a filament and e-beam heating. The temperature is monitored via a K-type thermocouple attached to the manipulator. The chamber is pumped by a combination of turbo pumps and diffusion pumps to achieve a base pressure  $\sim 10^{-10}$  mbar, allowing the prepared surfaces to remain free from contamination for several hours. This high pumping speed helps when depositing material as any non-adsorbed atoms are quickly removed when the deposition source is turned off. The pumping for the ion column is provided by a diffusion pump. The separate arrangement of the pumping means the required difference of 3–4 orders of magnitude for data acquisition and operation of ion source can be achieved.

The chamber is also equipped with a retractable LEED optic (Omicron), a TC-50 thermal gas cracker (OAP), ion gun for sample preparation, a dual anode x-ray source (VG,  $\text{Al}_{k\alpha}$ ,  $\text{Mg}_{k\alpha}$ ), and a 100mm concentric hemispherical analyser for use with XPS and AES, which requires an electron gun.

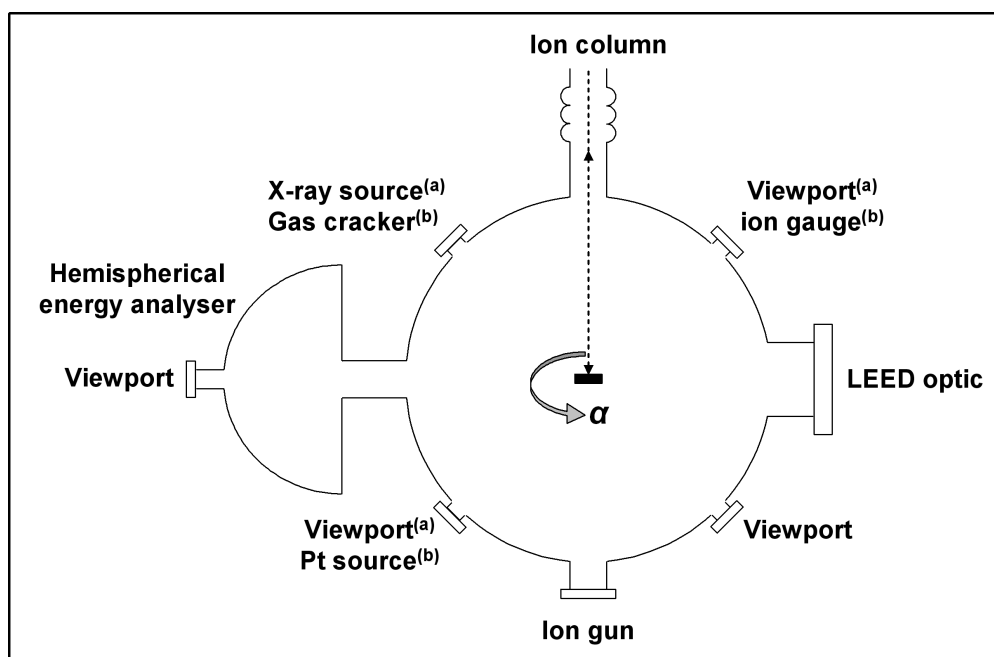


Figure 3.3: Top down schematic of the CAICSS system at Warwick, with key components labelled

## 3.2 ELVIS

The ELVIS chamber is so named for the techniques available on the system, listed below:

- High Resolution Electron Energy Loss Spectroscopy (HREELS)
- Low Energy Electron Diffraction (LEED)
- Ultra-violet Photoelectron Specstroscopy (UPS)
- Inverse Photoemission Specstroscopy (IPES)
- X-ray Photoelectron Specstroscopy (XPS)

All of these techniques allow for studies of different aspects of the electronic properties of the surface of a material. Due to the design of the chamber, all of these techniques are on retractable mounts so that no instrument for one technique will interfere with another whilst in use. The LEED optic is provided by Omicron, XPS equipment is manufactured by Omicron and is a fully computer controlled system with a dual  $\text{Al}_{k\alpha}$  and  $\text{Mg}_{k\alpha}$  anode. The IPES equipment is manufactured by PSP, and the UPS system was built in-house. The manipulator in this chamber is capable of polar rotation, with a large range of motion in  $z$ , to allow for change in level to access the different techniques. The sample holder allows for e-beam heating in the range 20 – 800 °C, monitored by a k-type thermocouple. The base pressure of the system is  $\sim 10^{-10}$  mbar, pumped by two turbo pumps and backed by rotary pumps. Figure 3.4 shows a schematic drawing of the ELVIS chamber, denoting key instrumentation.

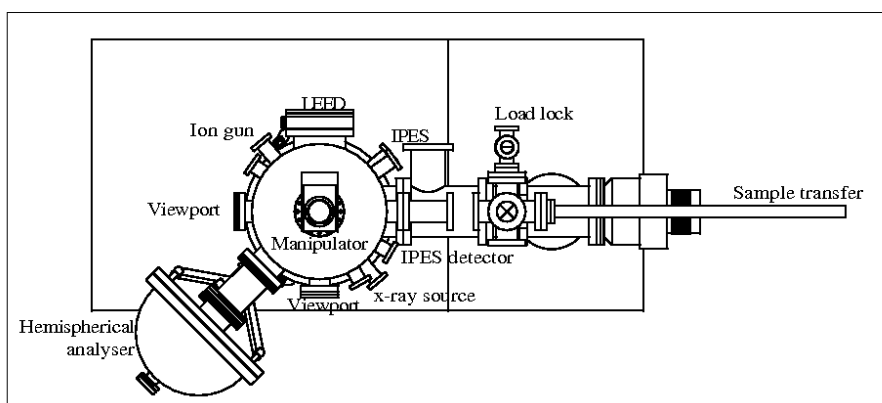


Figure 3.4: Top down schematic of the ELVIS system, showing key instrumentation in upper level.

## 4 Current Results

### 4.1 Valence band offsets of ScN systems

ScN is an important material in the III-V semiconductor industry. It exhibits some very useful physical properties, including high hardness and high melting point, which coupled with a wide energy gap leads to a promising option for ohmic contacts to other group III nitrides. These properties also make a promising prospect for use as buffer layers in other material systems [27, 28, 29].

#### 4.1.1 XPS observations

XPS measurements were performed on samples of different ScN layer thickness using a Scienta ESCA 300 spectrometer at NCESS [24]. The samples were probed using a photon beam with incident energy of  $h\nu = 1486.6$  eV produced by a rotating  $\text{Al}_{k\alpha}$  source and passed through a monochromator. The emitted photoelectrons were analysed using a 300mm mean radius hemispherical analyser with slit width 0.8 mm, and pass energy set at 150 eV. This gave an effective resolution of 0.45 eV, caused by a Gaussian convolution of the analyser broadening with the natural line width of the source (0.27 eV). All energies are referenced to the Fermi level. The Fermi level position was calibrated using the Fermi edge of an ion bombarded silver reference sample that is regularly used to calibrate the system.

Previous results have shown that the peaks visible in Figure 4.1 to be due only to Sc-Sc bonding and Sc-N bonding [30]. With the results achieved it is not possible to reconcile this exactly, as the ratio for peak intensity due to the lower binding energy doublet peak at 400 eV is incorrect for a p orbital splitting. The ratio should be 2:1, but this is not the case, and cannot be accounted for without the inclusion of extra peaks in this region.

Currently the doublet at 403.44 eV is thought arise from Sc-O bonding, the presence of this signal after annealing at 500°C, with a changed peak shape, matching the change in the O1s signal leads to this conclusion. It can also be seen that the peak has shifted in energy downward to 402.23 eV. The existence of the O1s signal after the anneal cycles suggests that a different surface preparation method is needed to obtain a clean surface, and thus determine whether the peak at 403.44 (402.23) eV is infact due to Sc-O bonding. If this proves not to be the case, then a further question about the exact make up of the Sc2p peak is introduced. If the lower binding energy peak at 400.45 eV is found to just be Sc-N bonding, then the difference in peak ratio needs to be explained, as it does not follow the quantum ratio of 2:1 as would be expected for

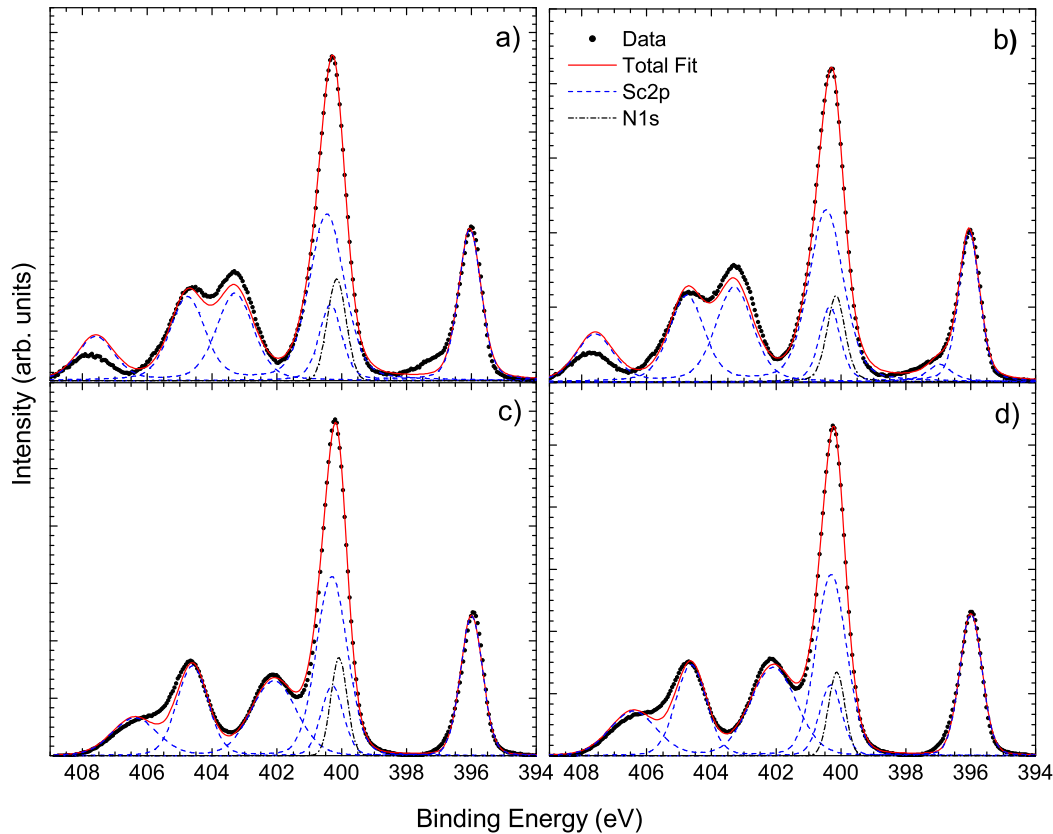


Figure 4.1: XPS spectra for sample JH35, in the  $\text{Sc}_{2p}$  region under different preparation conditions and take off angle (TOA). a) As loaded with  $30^\circ$  TOA, b) As loaded  $90^\circ$  TOA, c)  $2 \times 2$  hr anneal at  $500^\circ\text{C}$  with  $30^\circ$  TOA, d)  $2 \times 2$  hr anneal at  $500^\circ\text{C}$  with  $90^\circ$  TOA.

a  $p$  orbital. The analysis containing three component peaks to create this particular peak is complex, but does explain the situation more closely than a single peak can.

As can be seen on the lowest binding energy peak (attributed to Sc-N bonding) at 396.14 eV, there is a change in the higher binding energy tail after annealing. Upon annealing, the tail disappears from the signal, which is attributed to oxygen and other contaminants on the surface of the material being removed from the surface by annealing.

This preliminary work is a good lead in to work on InN, as it provides a complex system to understand, such as the N1s peaks in InN, which are sometimes not obviously visible compared to the background level of other materials. Since the ScN sample is not wurtzite it would be also be interesting to look at the use of ScN as a buffer layer for the growth of InN, and look at the effect on the structure of the InN grown.

## 4.2 CAICISS simulation

Previous work on the atomic structure of InN(0001) has been performed using the CAICISS system at Warwick. The samples in use for these previous experiments were prepared in situ by atomic hydrogen cleaning (AHC). Molecular hydrogen was thermally cracked with  $\sim 50\%$  efficiency using a TC-50 atomic hydrogen source, for two 10 kL doses of  $H_2$ , the first at room temperature and the second at  $175^\circ\text{C}$ . The samples were then annealed without exposure to hydrogen at  $300^\circ\text{C}$  for 2 h. Initial experiments were performed using CAICISS to determine the polarity of the samples used, by comparing features at different polar scattering angles along the  $[1000]$  azimuth.

Further samples with known polarity were then prepared, with RHEED being performed in the growth chamber and XPS[31] data being taken ex situ. This data led to an adlayer model for the structure of the InN surface of  $c$ -plane InN. The XPS data led to the determination of  $\sim 3.4$  ML of In at the surface. CAICISS was then performed on these samples to determine the atomic structure of this adlayer model. The CAICISS results as shown in Figure 4.2 show the model that was produced demonstrates a  $(\sqrt{3} \times \sqrt{3})R30^\circ$  periodicity in the surface. This is not necessarily observed in the LEED due to highly mobile In atoms at the surface [10].

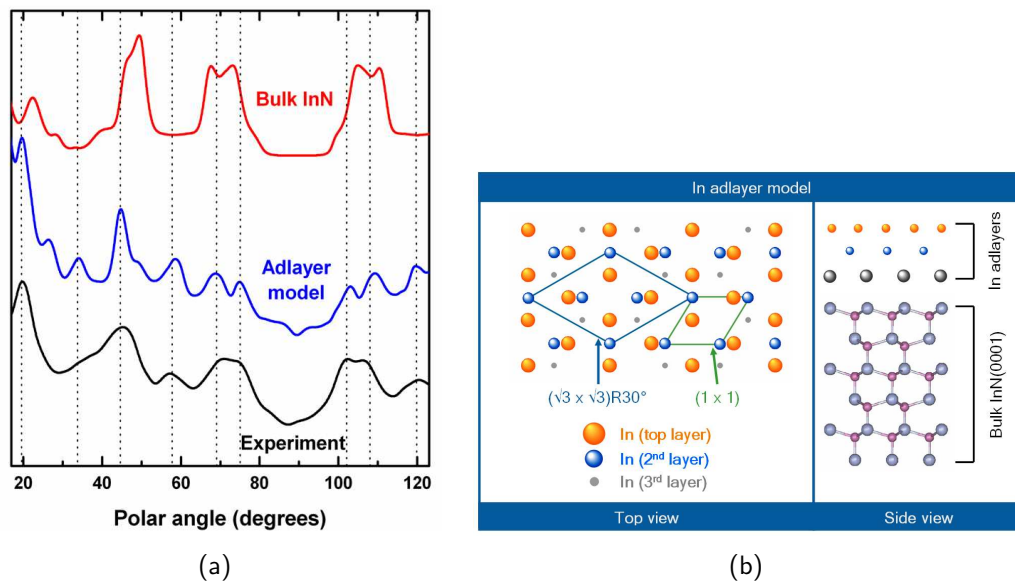


Figure 4.2: (a) CAICISS experimental data compared with a bulk terminated InN and an adlayer model with 3 adlayers of In. (b) Structural models showing the top and side views of the In-adlayer surface reconstruction for In-polarity  $c$ -plane InN surface. There are three layers of In on top of the In-terminated bulk InN. The topmost layer consists of  $4/3$  ML of In with  $(\sqrt{3} \times \sqrt{3})R30^\circ$  periodicity [10].

Work is currently underway testing a new cleaning method of HCl etching. The sample is etched in a 10 % HCl solution for 10 mins, then cleaned in de-ionised water

and cleaned with an ultrasonic device for a further 10 mins, before being placed in the sample chamber. The sample is then left to anneal at 150 °C for 12 h, and annealed again at 350 °C for 30 mins. A  $(1 \times 1)$  LEED pattern at high energy (350 eV) with high background was observed.

This method is currently proving unsuccessful, with no distinct LEED pattern observed at lower energies. This suggests that the surface is not ordered, and multiple anneal cycles have yet to produce a clean surface. Because of this, a return to the previous experimental data to re-evaluate the simulations is being undertaken. This involves modelling the different adlayer structures possible with differing interlayer spacings to verify that the previously obtained model with the interlayer spacings used there is the best fit to the data.

The structure has so far been modelled with one, two and three adlayers of In at the surface of In-polarity InN(0001). Figure 4.3 illustrates the current models, and shows where they do not match the data very well, meaning that these models are not yet the correct ones, with extra scattering geometries required to generate the peaks at 21°, 45°, 57°, and 102°. The addition of a  $(\sqrt{3} \times \sqrt{3})$  reconstructed adlayer on top of the third layer should more closely match the previous data. This will then require the interlayer spacings to be optimised, a task currently being performed without this reconstructed layer, to optimise features that are currently visible in both the experimental data and models.

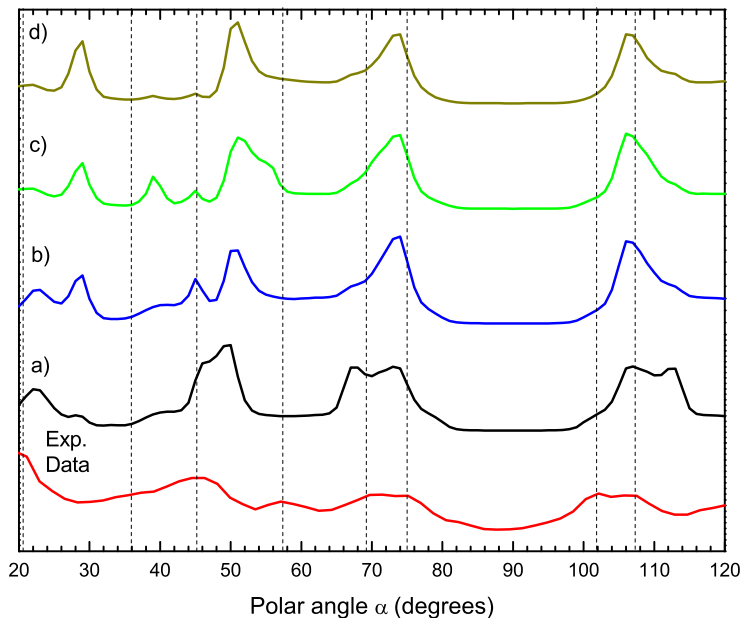


Figure 4.3: In-terminated InN(0001) CAICISS spectra, with the experimental result, and the simulation of multiple adlayers shown. a) ideal bulk terminated InN, b) 1 adlayer at 2.86Å above the bulk termination, c) 2 adlayers at 2.86 and 4.26Å above the bulk, and d) 3 adlayers at 2.86, 4.26 and 7.12Å above the bulk. The dotted line identifies key features in the experimental data.

## 5 Research Plan

### 5.1 April 2009 – June 2009

- Determine the atomic structure of (0001) and (000 $\bar{1}$ ) wurtzite InN, using the CAICISS system at warwick.
- Develop cleaning procedure for InN surfaces and measure the structural and electronic effects of these procedures, including but not limited to HCl etching (to be performed at Warwick and NCESS), N ion bombardment and atomic hydrogen cleaning.
- Continuation and completion of the ScN band offset study at NCESS in June.

### 5.2 July 2009 – Sept 2009

- Characterisation of material deposition including Mg deposition for use in influencing *p*-type doping of InN surfaces / interfaces.
- Investigate the electronic properties of different metals deposited as contacts to the surface of InN, determination of Schottky barrier heights if applicable.
- Investigate sulphur passivation of the InN surface, such that it can be removed from vacuum and still maintain its properties without oxidation effects.

### 5.3 Oct 2009 – Dec 2009

- Investigate the effect of high-K dielectrics on the surface of InN with respect to reducing gate leakage current, interface charge and process temperature. This will be studied for the use of InN as a channel material in high speed transistors and as such needs good control of these properties.
- Evaluate electronic and chemical effects of exposure of the surface of InN to different chemicals, e.g. methanol, water and acetone.
- Determine the atomic structure of (11 $\bar{2}$ 0) and (1 $\bar{1}$ 00) wurtzite InN and (001) and (111) zinc blende InN in the CAICISS system at Warwick.

## A Key Text Review

1. I. Mahboob, T.D. Veal, C.F. McConville, Hai Lu and W. J. Schaff, *Intrinsic electron accumulation at clean InN surfaces*, Phys. Rev. Lett. **92** (2004), 036804
2. D. Segev and C. G. Van de Walle, *Origins of Fermi-level pinning on GaN and InN polar and nonpolar surfaces*, Europhys. Lett. **76** (2006) 305; *Surface reconstructions on InN and GaN polar and nonpolar surfaces*, Surf. Sci. **601** (2007) L15.
3. T. D. Veal, P. D. C. King, M. Walker, C. F. McConville, Hai Lu, W. J. Schaff, *In-adlayers on nonpolar and polar InN surfaces: Ion scattering and photoemission studies*, Physica B **401-402** (2007) 351.
4. J. E. Northrup, J. Neugebauer, R. M. Feenstra and A. R. Smith, *Structure of GaN(0001): The laterally contracted Ga bilayer model*, Phys. Rev. B **61** (2000) 9932.
5. H. Niehus, W. Heiland, and E. Taglauer, *Low energy ion scattering at surfaces*, Surf. Sci. Rep. **17** (1993) 213.

## A.1 Intrinsic electron accumulation at clean InN surfaces

In this paper by Mahboob *et al.* [5] high resolution electron energy loss spectroscopy is used to investigate conduction band electron plasmon excitations. This is in contrast to earlier work that required metal deposition on the surface of InN [32, 33]. As a result, these previous studies were unable to characterise the free surface, in contrast to Mahboob's work which characterised the free surface. The author uses a semi-classical dielectric theory to produce simulations which are then fitted to the data presented. These simulations were used in conjunction with creating a plasma dead layer to fit the data correctly.

The author then illustrates the variation of plasma frequency and electron effective mass at the fermi level as a function of the electron concentration. The effective mass of the electron at the conduction band minimum is used from the work of Wu *et al.* [34] and the value given is  $m_0^* = 0.007m_e$ . The author makes use of Kane's **k.p** theory [12], as in many other works, due to its relevance for modelling the non-parabolic conduction band that is present in InN.

The origins of the accumulation layer are discussed in the closing paragraphs of the paper. The existence of positively charged donor-type surface states is used to explain the accumulation layer. These surface states only arise when they, lie below the branch-point energy,  $E_B$ , for that material. This is the case for InN due to its small band gap at the  $\Gamma$ -point, whereas the branch-point energy falls closer to the centre of the gap in the complex band structure.

This bandstructure, calculated by Bechstedt *et al.* [35], indicates that the  $\Gamma$ -point CBM is much lower than the overall conduction band, lending weight to the evidence for the accumulation layer. To finish the author indicates the presence or not of an accumulation layer in other In containing materials, such as InAs, InP and InSb.

The discovery of this electron accumulation layer has proved to be very important and has driven further investigations to determine if this phenomenon is present at all InN surfaces [36].

## A.2 Origins of Fermi-level pinning on GaN and InN polar and nonpolar surfaces

This paper by Segev *et al.* [6] investigates a theoretical approach to determining the effect of different growth conditions on different surfaces of both InN and GaN. Potential device applications, such as high-electron mobility transistors (HEMTs), are mentioned, with relevance to this work due to the high surface condition sensitivity. This surface sensitivity is particularly important as it is thought the surface is the main

source of electrons for the two-dimensional electron gas [37]. The authors employ DFT using the LDA, or with a generalized gradient approximation (GGA) [38]. The advantages and disadvantages of each method are briefly discussed, explaining the difficulty of interpretation of the results provided by either of these methods.

The potentials used for each material and other important details including lattice parameters are then given, to allow for reproduction of the calculations for verification.

The authors then move on to discuss the effects on polar surfaces under moderate Ga(In)/N ratios and the results provided there, before moving on to nonpolar surfaces under moderate conditions. For these moderate conditions the authors find a dimer structure to be the most stable, as evidenced by Northrup and Neugebauer [39]. The formation of this dimer structure is then explained, giving an unoccupied Ga-dangling-bond state  $\sim 0.7$  eV below the CBM for  $m$  plane and two unoccupied states  $\sim 0.5$  eV below the CBM for  $a$  plane. These dangling bonds are similar to those for the polar surface and result in a similar Fermi-level pinning on  $n$ -type GaN. The author then states that the occupied states are different to those in polar surfaces, they do not create levels within the band gap, and overlap with the valence band.

In the second paper [40] the authors take a similar approach to that of the first paper. The focus of this paper is the surface reconstructions under the different conditions for both the polar and nonpolar surfaces however. The relevant atomic parameters are given initially, of  $a = 3.22 \text{ \AA}$ ,  $c/a = 1.623$  and  $u = 0.377$  for GaN, and  $a = 3.58 \text{ \AA}$ ,  $c/a = 1.617$  and  $u = 0.379$  for InN, stated to be within 1% of experimental values, although no source for this is stated. The authors also describe the system they are simulating in more detail including the formulae used for surface energy calculations and chemical potentials for the different cation and anion states.

It was found that for the GaN(0001) and GaN(000 $\bar{1}$ ) systems that the structures and energies were in agreement with previous published materials. It shown for the GaN(0001) system that as the Ga potential increases there was a transition from a  $(2 \times 2)$  N-adatom structure to a  $(2 \times 2)$  Ga-adatom reconstruction, and onto a Ga-bilayer structure under Ga-rich conditions. The GaN(000 $\bar{1}$ ) showed a different transition, evolving from a  $(2 \times 2)$  Ga-adatom structure to a  $(1 \times 1)$  reconstruction with Ga directly atop N atoms with increasing Ga/N ratio.

Similar results for the InN(0001) system were found, except that there were no reconstructions involving N-adatoms under N-rich conditions. This means that the  $(2 \times 2)$  structure remains stable even under In-poor conditions. The authors then suggest that this finding indicates a trend of destabilisation of the N adatom structure with increasing cation atomic number in III-nitride compounds, due to the reported data for AlN suggesting that the  $(2 \times 2)$  N-adatom reconstruction remained stable

across almost the entire range of Al chemical potentials. For the InN(000 $\bar{1}$ ) surface the authors found the In terminated ( $1 \times 1$ ) reconstruction to be stable over the entire range of In potentials. This surface is one with a monolayer of In on the top, resulting in a metallic surface, which is lower in energy to other metallic structures. The authors report that the ( $2 \times 2$ ) reconstruction is not stable for any In chemical potential, in contrast to that of GaN(000 $\bar{1}$ ).

For non-polar surfaces ( $m$  and  $a$  plane) the authors found that the Ga-N dimer structure was the most stable over a large range of Ga potentials, with some previously unseen reconstructions for the Ga-rich conditions on the  $m$  plane. For  $a$  plane a stable ( $1 \times 1$ ) reconstruction was observed. For InN the  $m$  and  $a$  planes were found to be similar to GaN, with In-N dimers stable at moderate In/N ratios, and metallic reconstructions similar to those for GaN at high In/N ratios.

Finally the authors noted an interesting feature of polarity inversion among the topmost layer of the surfaces, a phenomenon which could be investigated with CAICISS.

### A.3 In-adlayers on nonpolar and polar InN surfaces: Ion scattering and photoemission studies

In this work by Veal *et al.* [10] the surface structure is determined by both ion scattering surveys and photoemission studies. After describing the preparation of the samples the authors proceed to present ion scattering data from an In-polarity  $c$ -plane InN sample, with corresponding simulations. The author notes that some key features in the experimental data were not reproduced in the calculated spectrum for a bulk terminated InN sample with respect to polar angle. Additionally some other features at  $\sim 20^\circ$ ,  $\sim 45^\circ$ ,  $\sim 69-75^\circ$  and  $\sim 102-108^\circ$  were calculated a few degrees away from where they were observed experimentally. This led to the production of other trial structures to reconcile this lack of agreement.

The author then reports that the best agreement between experimental data and the simulated spectra arose when the bulk-terminated structure is terminated with three layers of In, with a  $\frac{4}{3}$  ML coverage of In in the topmost layer, which also shows a  $(\sqrt{3} \times \sqrt{3})R30^\circ$  periodicity. Reasons for why this structure fits, including the matching of the peak at  $58^\circ$  being due to shadowing of In in the topmost layer onto atoms in the second layer. It is also reported that the structure is consistent with the observation of  $\sim 3.4$  ML of In-adlayers determined from the In:N ratio observed in photoemission spectra, and the  $(\sqrt{3} \times \sqrt{3})R30^\circ$  reconstruction being observed in RHEED. The CAICISS chamber was only able to see the integral order spots with high background in LEED, suggesting a disordered surface but not ruling out the  $(\sqrt{3} \times \sqrt{3})R30^\circ$  periodicity. The authors explain that the simulated spectra still produces angularly narrower peaks

than the experimental data, due to the possibility of mobile In atoms at the surface, which could result in the presence of rapidly moving domain boundaries, and leading to the  $(1 \times 1)$  LEED pattern observed with a high background intensity.

In coverage on the clean surface of  $a$ -plane InN was investigated using XPS to determine whether In adlayers were again present. The calculated intensity ratios, from the core-level peaks areas, were determined to be 1.9 and 2.8 at  $90^\circ$  and  $30^\circ$  respectively. This increased ratio for  $30^\circ$  indicates the presence of an In-rich surface at the  $a$ -plane.

The authors then report that the surface In-coverage of  $a$ -plane InN is  $\sim 1.4$  ML lower than that of the In polarity  $c$ -plane which has  $\sim 3.4$  ML of In above the In-terminated bulk. XPS results are also reported to show that the VBM to surface Fermi level separation in InN is not dependent on orientation of the crystal, which was compared to DFT calculations of the VB-DOS

#### A.4 Structure of GaN(0001): The laterally contracted Ga bilayer model

This paper presented by Northrup *et al.* [41] discusses a theoretical approach to determining a structural model for GaN(0001). The author begins by introducing the findings of experimental results suggesting that during and post MBE growth a different number of reconstructions are observed, changing from  $2 \times 2$ , to  $5 \times 5$ ,  $4 \times 6$  and finally to a pseudo- $1 \times 1$  structure, found through the termination of growth under Ga-rich conditions. The author then notes some key findings with regards to the pseudo- $1 \times 1$  structure in that whilst the STM appears to show the same corrugation pattern and lateral spacing as bulk GaN[42], electron diffraction experiments show beam intensity at satellite spots, indicating the actual lattice vectors of the surface unit cell are much larger than those corresponding to the  $1 \times 1$  unit cell.

The author gives evidence that indicates the surface consisting of a laterally contracted bilayer of Ga is the most stable structure, and finds that the energy barrier level is  $0.02 \text{ eV} / 1 \times 1$ , showing that the bilayer structure contains  $\sim 2.3$  ML of Ga above the Ga-terminated GaN bilayer. Discussion of the  $2 \times 2$  structure follows this, with the suggestion that this reconstruction is usually a consequence of N adatoms, from the growth conditions, or that it can be obtained during growth with As present on the surface.

Returning to the pseudo- $(1 \times 1)$  structure the authors discuss how the theory must confront identification of a structure that is consistent with experimental results and stable with respect to other possible reconstructions. In particular the authors discuss how previous work indicated structures with 1 or 2 ML of excess Ga, with  $(1 \times 1)$  translation symmetry are not as stable as the  $(2 \times 2)$  Ga-adatom model under Ga-rich

conditions, but with considerable tensile stress and would be expected to contract. The authors present calculations to show that a laterally contracted Ga-bilayer is more stable than the  $(2 \times 2)$  Ga adatom model by at least  $0.25 \text{ eV} / (1 \times 1)$  in the Ga-rich limit.

The authors then use a  $(\sqrt{3} \times \sqrt{3})$  unit cell to model a laterally contracted adlayer structure, which was found to be effective in producing an accurate model. For the bilayer model two different registries were modelled, and their average vertical separations were virtually identical, thus suggesting the structure is independent of the registry with the substrate. Comparing with the electron diffraction data the authors discuss that it would be energetically favourable and consistent to form an incommensurate laterally contracted bilayer model, but still observing the  $(1 \times 1)$  corrugation in the STM, attributed to mobile Ga atoms at the surface. The mobile topmost layer atoms is something also suggested in the work by Veal *et al.* for InN [10].

## A.5 Low energy ion scattering at surfaces

This review by Niehus *et al.* [18] covers many different aspects of low energy ion scattering, vitally important to this project as CAICISS, a LEIS technique, will be used extensively to study clean and adsorbate covered InN surfaces.

The authors begin by introducing the topic of surface science and its applications, and moves onto discussing the theory behind ion scattering. From here they show how  $180^\circ$  scattering geometry simplifies data analysis. The advantages of LEIS, in particular it's surface specificity, are introduced. The high degree of surface specificity makes LEIS a very good technique for determining the surface structure of crystalline materials, such as InN. Given that LEIS is low energy, it is also a largely non-destructive technique.

The authors then move on to introduce computational modelling ion scattering data. The particular simulation packages covered within this review are MARLOWE and FAN. MARLOWE is a 3D forward scattering Monte Carlo simulation package, and is as such not particularly useful for this project, due to its computational inefficiency. FAN on the other hand is a 3D backscattering package and is not based on Monte Carlo calculations. The FAN code simulates ion scattering experiments by creating a "fan" of trajectories from each atom within the trial structure. Both the possible incident and outgoing trajectories are calculated for each atom over a given range of scattering and polar angles. Only trajectories which will reach the detector are calculated, meaning that the code is significantly more efficient than its Monte Carlo and molecular dynamic counterparts.

FAN was specifically designed for backscattering applications such as CAICISS [43], therefore making it an ideal choice for the computational analysis of ion scattering data in this project.

In the next chapters the author discusses the experimental side of performing ion scattering. Covering ICISS, DRS, RBS and other spectroscopies. The different analysis methods are covered, including TOF analysis. The author then proceeds to discuss structural damage caused by ion scattering, the effect of sputtering away atoms from the surface due to the collision of ions with the atoms.

## References

- [1] J. Wu et al., Appl. Phys. Lett. **80**, 3967 (2002).
- [2] J. Wu et al., J. Appl. Phys. **94**, 4457 (2003).
- [3] C. J. Neufeld et al., Appl. Phys. Lett. **93**, 143502 (2008).
- [4] P. D. C. King et al., Phys. Rev. B **77**, 045316 (2008).
- [5] I. Mahboob, T. D. Veal, C. F. McConville, H. Lu, and W. J. Schaff, Phys. Rev. Lett. **92**, 036804 (2004).
- [6] D. Segev and C. G. V. de Walle, EPL (Europhysics Letters) **76**, 305 (2006).
- [7] W. Walukiewicz et al., J. Phys. D: Appl. Phys. **39**, R83 (2006).
- [8] J. Wu et al., Appl. Phys. Lett. **80**, 4741 (2002).
- [9] M. Walker, T. D. Veal, H. Lu, W. J. Schaff, and C. F. McConville, Phys. Stat. Sol. C **2**, 2301 (2005).
- [10] T. D. Veal et al., Physica B **401-402**, 351 (2007).
- [11] B. Ridley, *Quantum Processors In Semiconductors*, Oxford Science Publications, 1993.
- [12] E. O. Kane, J. Phys. Chem. Solids **1**, 249 (1957).
- [13] B. Nag, *Electron Transport In Compound Semiconductors*, Springer-Verlag, 1980.
- [14] P. D. C. King, T. D. Veal, and C. F. McConville, Phys. Rev. B **77**, 125305 (2008).
- [15] D. P. Woodruff and T. A. Delchar, *Modern Techniques Of Surface Science - Second Edition*, Cambridge University Press, 1994.
- [16] L. Rosenberger, R. Baird, E. McCullen, G. Auner, and G. Shreve, Surf. Interface Anal. **40**, 1254 (2008).
- [17] T. Kuzushita, A. Murata, A. Yamamoto, and T. Urano, Appl. Surf. Sci. **254**, 7824 (2008), 9th International Conference on Atomically Controlled Surfaces, Interfaces and Nanostructures 2007 (ASCIN-9).
- [18] H. Niehus, W. Heiland, and E. Taglauer, Surf. Sci. Rep. **17**, 213 (1993).
- [19] G. Molière, Z. Naturforsch **2a**, 133 (1947).
- [20] S. Cruz, E. Alonso, R. Walker, D. J. Martin, and D. G. Armour, Nuclear Instruments and Methods **194**, 659 (1982).
- [21] J. Ziegler, J. Biersack, and U. Littmark, *The stopping and ranges of ions in solids, Vol. 1*, Pergamon(New York), 1985.

- [22] M. Draxler, M. Walker, and C. McConville, Nucl. Inst. Meth. B **249**, 886 (2006), Ion Beam Analysis - Proceedings of the Seventeenth International Conference on Ion Beam Analysis.
- [23] D. P. Smith, Surf. Sci. **25**, 171 (1971).
- [24] The National Centre for Electron Spectroscopy and Surface Analysis, <http://www.dl.ac.uk/NCESS/xps/xps.htm>.
- [25] P. Bailey, T. C. Q. Noakes, and D. P. Woodruff, Surf. Sci. **426**, 358 (1999).
- [26] M. Walker, *Low Energy Ion Scattering Studies of Metal, Metal Oxide and Alloy Surfaces*, PhD thesis, University Of Warwick, 2006.
- [27] M. A. Moram, Y. Zhang, M. J. Kappers, Z. H. Barber, and C. J. Humphreys, Appl. Phys. Lett. **91**, 152101 (2007).
- [28] M. Moram et al., J. Cryst. Growth **308**, 302 (2007).
- [29] M. Moram et al., J. Cryst. Growth **310**, 2746 (2008).
- [30] L. Porte, J. Phys. C: Solid St. Phys. **18**, 6701 (1985).
- [31] T. D. Veal et al., Phys. Rev. B **76**, 075313 (2007).
- [32] K. A. Rickert et al., Appl. Phys. Lett. **82**, 3254 (2003).
- [33] H. Lu, W. J. Schaff, L. F. Eastman, and C. E. Stutz, Appl. Phys. Lett. **82**, 1736 (2003).
- [34] J. Wu et al., Phys. Rev. B **66**, 201403 (2002).
- [35] F. Bechstedt et al., Phys. Stat. Sol. A **195**, 628 (2003).
- [36] P. D. C. King et al., Appl. Phys. Lett. **91**, 092101 (2007).
- [37] J. P. Ibbetson et al., Appl. Phys. Lett. **77**, 250 (2000).
- [38] J. P. Perdew, K. Burke, and M. Ernzerhof, Phys. Rev. Lett. **77**, 3865 (1996).
- [39] J. E. Northrup and J. Neugebauer, Phys. Rev. B **53**, 10477 (1996).
- [40] D. Segev and C. G. Van de Walle, Surf. Sci. **601**, L15 (2007).
- [41] J. E. Northrup, J. Neugebauer, R. M. Feenstra, and A. R. Smith, Phys. Rev. B **61**, 9932 (2000).
- [42] A. Smith et al., J. Vac. Sci. Tech. B **16**, 2242 (1998).
- [43] H. Niehus and R. Spitzl, Surface and Interface Analysis **17**, 287 (1991).